Ultrafast lattice response of photoexcited thin films studied by X-ray diffraction

Daniel Schick,[1,2] Marc Herzog,[1,3] André Bojahr,[1] Wolfram Leitenberger,[1] Andreas Hertwig,[4] Roman Shayduk,[2,5] and Matias Bargheer[1,2,a)]
[1]*Institut für Physik und Astronomie, Universität Potsdam, Karl-Liebknecht-Straße 24-25, 14476 Potsdam, Germany*
[2]*Helmholtz-Zentrum Berlin für Materialien und Energie GmbH, Wilhelm-Conrad-Röntgen Campus, BESSY II, Albert-Einstein-Straße 15, 12489 Berlin, Germany*
[3]*Abteilung Physikalische Chemie, Fritz-Haber-Institut der Max-Planck-Gesellschaft, Faradayweg 4-6, 14195 Berlin, Germany*
[4]*Bundesanstalt für Materialforschung und -prüfung, Unter den Eichen 87, 12205 Berlin, Germany*
[5]*Deutsches Elektronen-Synchrotron DESY, Notkestraße 85, 22607 Hamburg, Germany*

(Received 5 September 2014; accepted 28 October 2014; published online 18 November 2014)

Using ultrafast X-ray diffraction, we study the coherent picosecond lattice dynamics of photoexcited thin films in the two limiting cases, where the photoinduced stress profile decays on a length scale larger and smaller than the film thickness. We solve a unifying analytical model of the strain propagation for acoustic impedance-matched opaque films on a semi-infinite transparent substrate, showing that the lattice dynamics essentially depend on two parameters: One for the spatial profile and one for the amplitude of the strain. We illustrate the results by comparison with high-quality ultrafast X-ray diffraction data of $SrRuO_3$ films on $SrTiO_3$ substrates. © *2014 Author(s). All article content, except where otherwise noted, is licensed under a Creative Commons Attribution 3.0 Unported License*. [http://dx.doi.org/10.1063/1.4901228]

I. INTRODUCTION

Pump-probe experiments measure the coupling of various degrees of freedom on their intrinsic timescale of femtoseconds to nanoseconds. An increasingly powerful toolbox of time-resolved experimental techniques—ranging from Raman scattering over magneto-optical Kerr (MOKE) measurements[1,2] to angular-resolved photoelectron spectroscopy (ARPES)[3]—is applied to directly monitor specific subsystems in solids (charge, spin, orbital, and lattice). The majority of experiments are conducted on thin film samples which have been designed to exhibit the phenomena of interest. Especially for opaque layers, the high energy density deposited in the thin film by the pump pulse not only leads to strong and interesting changes, e.g., in the magnetization or electronic properties, but also to considerable dynamics of the underlying crystal lattice.[4–6]

Since the pioneering work of Thomsen *et al*. in 1984 and 1986[7,8] Brillouin scattering methods with optical light have been steadily improved and allow for following the evolution of photoexcited coherent strain pulses.[7,9] In general, optical light is only an indirect probe for lattice motion, since it is exclusively sensitive to the dielectric function of matter, which is usually strongly modified in pump-probe experiments by the substantial perturbation of the electronic system. More than a decade ago, ultrafast X-ray diffraction (UXRD) techniques emerged as a versatile tool to monitor photoexcited lattice dynamics directly on the relevant length and time scales.[10–16] Recent UXRD studies established this technique for reconstructing photoexcited coherent strain pulses[17] and used it to determine the underlying mechanism for exciting the

a)Electronic mail: bargheer@uni-potsdam.de; URL: http://www.udkm.physik.uni-potsdam.de.

 © Author(s) 2014

atomic motion[17–23] or to study phonon damping mechanisms.[24] In addition, ultrafast electron diffraction also reveals the structural dynamics of photoexcited condensed matter; however, this technique exclusively probes the surface-near regions of the sample.[25] Despite this multitude of experimental studies and although the seminal work by Thomsen *et al.* has been cited and elaborated more than 500 times,[8] a comprehensive study of the ultrafast lattice dynamics and its direct signature in UXRD data for the common case of an opaque thin film on a semi-infinite transparent substrate are still missing in the literature. In our opinion, the lattice dynamics form an important basis of all electronic dynamics and especially for solids with complex couplings and collective phenomena a thorough assessment of the lattice dynamics is mandatory.

In this contribution, we choose the "bad metal" $SrRuO_3$[26] as a prototypical optically opaque thin-film material with a very short electron-phonon coupling time which was deposited on the standard substrate material $SrTiO_3$. We discuss the lattice dynamics after photoexcitation in the two limiting cases, where the photoinduced spatial stress profile $\sigma(z)$ decays on a lengths scale ζ larger and smaller than the film thickness d. Working out the standard thermoelastic model[8] in the Appendix and introducing universal temporal and spatial coordinates which are scaled by sound velocity v and film thickness d, respectively, we identify two essential parameters defining the lattice dynamics: $\delta = d/\zeta$ for the spatial profile and α for the amplitude of the strain, where α incorporates all acoustic and thermoelastic parameters. The model correctly describes signatures in the UXRD data for $\delta > 1$ which are at first sight surprising: The Bragg peak of the opaque layer first shifts to larger angles, indicating a compression of the film despite the expansive photoinduced stress. The intensity of this initial peak decreases and is transferred to a Bragg peak which emerges at smaller angles. For $\delta < 1$, the observed continuous shift to smaller angles is captured equally well by this model. We demonstrate an elegant way to measure the sound velocity in impedance-matched thin films, which is not easily accessible by other experiments, and discuss how to extract the other parameters from the experimental data. We use the model in its simplest form, for a perfect acoustic impedance match of the thin film and the underlying substrate, for instantaneous stresses driving the lattice dynamics, and for negligible heat diffusion in the sample structure.

In Sec. II, we briefly introduce the analytical model and discuss the predicted lattice dynamics in dependence of the four parameters d, v, δ and α. A detailed derivation of the thermoelastic model is given in the Appendix. Section III describes the experimental setup and results, which are further discussed and related to our analytical model in Sec. IV.

II. THEORY

The strain $\eta(z,t)$ in the one-dimensional thermoelastic response of a semi-infinite crystal due to a photoexcited stress $\sigma(z,t)$ can be well described by the continuum model of Thomsen *et al.*,[7,8] where z is the depth of the crystal and t is the time. We adopt this model and apply the same nomenclature for the case of an impedance-matched opaque film of thickness d on a transparent semi-infinite substrate. We assume an instantaneous formation of the thermal stress at $t=0$ with the same spatial profile as the photoexcitation (very short electron phonon coupling time in $SrRuO_3$)[27,28] and neglect heat diffusion which is not relevant on this ultrashort time scale; $\sigma(z, t \geq 0) = \sigma(z)$. The optical excitation of the opaque film has an exponential spatial profile following Lambert-Beer's law and is determined by the optical absorption depth ζ, but is abruptly ending at the film interface at the depth $z=d$. For the case of a very thick layer, $d \gg \zeta$, our model coincidences with the original work of Thomsen *et al.*

We introduce normalized unitless space $x = z/d$ and time $\tau = vt/d$ coordinates into our thermoelastic model, where v is the longitudinal sound velocity normal to the surface of the thin film. The derivation of the according differential equation (wave equation) after this coordinate transformation is described in the Appendix in detail. A perfect matching of the acoustic impedance $Z = v\rho$ (ρ—mass density) prohibits reflections at the interface. If the sound velocity in the film v and the substrate v_s are different, the amplitude of the sound and the temporal coordinate must be scaled accordingly. The solution $\eta(x,\tau)$ of this wave equation solely depends on two more parameters: a shape parameter $\delta = d/\zeta$ determining the spatial shape of

the lattice excitation; and a scaling factor α which determines the maximum amplitude of the static strain in the film: $\eta(0,\tau)=\alpha$, cf. Eq. (A22). Here, α collects all experimental parameters and material properties which influence the amplitude of lattice distortion of the thin film, such as its heat capacity, thermal expansion coefficient, and excitation fluence. See Table I for a complete list of all parameters.

The solution of the normalized strain $\bar{\eta}(x,\tau)=\eta(x,\tau)/\alpha$ is plotted in Fig. 1 for different values of the shape factor δ for varying normalized delays τ. The two upper panels (a) and (b) represent the solution for the two limiting cases $\delta \ll 1$ and $\delta \gg 1$, where the latter case corresponds to bulk material already discussed by Thomsen *et al*. The two lower panels (c) and (d) show the experimental cases $\delta < 1$ and $\delta > 1$ for the two films of different thickness as described below in the experimental part and discussion.

For $\delta \ll 1$, cf. Fig. 1(a), the photoexcited stress is spatially homogeneous in the opaque film. The resulting lattice dynamics can only start at the surface $x=0$ and interface $x=1$ of the film where the stresses are highly unbalanced. At the interface, a tensile strain front travels into the film which is compensated by a compressive strain front propagating into the substrate which has exactly the same integral strain for perfect impedance matching. At the film surface ($x=0$), the situation is essentially the same, however, the compressive strain front cannot propagate away from the film into the air and is therefore reflected back into the film as an expansion (open boundary condition). At the time $\tau=1$, all tensile strain fronts have traveled once through the film adding up to the maximum integral expansion of the layer which is $\eta_{\mathrm{lay}}(\tau=1)/\eta_{\mathrm{lay}}(\tau\geq 2)=1.5$, cf. Eq. (A26), independent of any physical parameter of the model. Any significant difference from this ratio would indicate a deviation of the initial assumptions of the analytical model, e.g., that the photoexcited stress is not instantaneous,

TABLE I. Definitions and units of all physical quantities and parameters of the analytical model.

Name		Description	Unit
z		Spatial coordinate (depth)	m
t		Temporal coordinate (time)	s
Q		Energy of a single laser pulse	J
A		Excited area of the sample surface	m^2
ζ		Optical absorption depth	m
C		Specific heat capacity	$\mathrm{J/(K\,m^3)}$
R		Optical reflectivity coefficient	1
B		Bulk modulus	Pa
ν		Poisson ratio	1
β		Linear thermal expansion coefficient	1/K
ρ		Mass density	$\mathrm{kg/m^3}$
d		Layer thickness	m
δ	$=d/\zeta$	Shape parameter	1
v	$=\sqrt{3\frac{1-\nu}{1+\nu}\frac{B}{\rho}}$	Longitudinal sound velocity	m/s
α	$=\frac{(1-R)3B\beta Q}{\zeta\rho v^2 AC}$	Scaling of excitation amplitude	m
$T(z)$		Initial temperature profile	K
$\sigma(z,t)$		Dynamical stress	Pa
$u(z,t)$		Dynamical displacement	m
x	$=z/d$	Normalized spatial coordinate	1
τ	$=vt/d$	Normalized temporal coordinate	1
$g(x)$		Spatial temperature profile	1
$f(x)$	$=-\frac{\partial}{\partial x}g(x)$	Source term of inhom. wave equation	1
$w(x,\tau)$	$=u(x,\tau)/(\alpha d)$	Normalized dynamical displacement	1
$\eta(x,\tau)$	$=\alpha\frac{\partial}{\partial x}w(x,\tau)$	Dynamical deformation (strain)	1

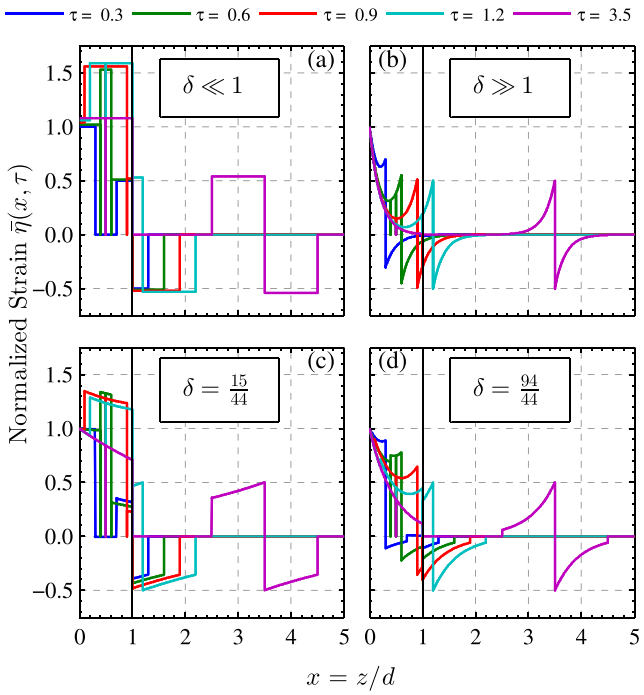


FIG. 1. The normalized strain $\bar{\eta}(x,\tau) = \eta(x,\tau)/\alpha$ is plotted for different shape parameters δ. (a) and (b) represent the limiting cases $\delta \ll 1$ and $\delta \gg 1$, respectively. (c) and (d) represent the experimental cases of $\delta = 15/44 = 0.34$ and $\delta = 94/44 = 2.14$, respectively. For an inhomogeneous spatial stress profile ($\delta > 1$), i.e., panels (b) and (d), the transducer layer ($0 \le x \le 1$) is negatively strained for $0 \le \tau < 1$. Note that in (a) the amplitude of $\bar{\eta}(x,\tau)$ is increased by 2% for each time step for better visibility.

because carrier transport during an extended electron-phonon coupling time occurs. For $\tau > 1$, the tensile strain front originating from the surface leaves the film and enters the substrate, ending the compressive strain in the substrate and starting the tensile part of the strain with the same amplitude $\eta(0, \tau \ge 2)/2$. At the same time, the tensile strain front originating at the film-substrate interface at $x = 1$ has reached the surface and is also reflected back into the film as a right-propagating compressive strain front, which reduces the strain at the surface to the final value $\eta(0, \tau \ge 2) = \alpha$. This compressive strain front propagates into the substrate at $\tau = 2$, marking the end of the bipolar strain pulse which keeps propagating in the substrate. The bipolar strain pulse has the same integral absolute strain as the remaining static strain in the thin film for $\tau \ge 2$.

For the second limiting case of $\delta \gg 1$, cf. Fig. 1(b), no photoexcitation occurs at the interface $x = 1$ but the thermal stresses within the layer are highly unbalanced following the exponentially decaying stress profile. Accordingly, at each point $0 \le x \le 1$ a left-propagating tensile strain front and a right-propagating compression strain front are triggered by the photoexcitation. These strain contributions add up to a stationary exponentially decaying component in the film and a propagating bipolar strain pulse with exponential edges. Again, at the time $\tau = 1$, the average strain in the layer is: $\eta_{\text{lay}}(1) = 1.5\,\eta_{\text{lay}}(\tau \ge 2)$, cf. Eq. (A26). A striking difference compared to the case of $\delta \ll 1$ is the occurrence of compressive strains in the opaque layer, although exclusively expansive stress was applied. This is a result of inhomogeneous excitation, where the larger expansion near the surface requires a compression of the adjacent material, which exceeds its own expansion. The occurrence of these transient compressive strains is solely determined by the shape factor δ and not by the scaling factor α or any other parameter. The experimental cases with the shape factors $\delta = 15/44$ and $\delta = 94/44$, see Figs. 1(c) and 1(d), share the dominant features of the two limiting cases as described above. In the Discussion section, we will show δ is experimentally derived.

III. EXPERIMENTAL SETUP AND RESULTS

We choose two thin films of the metallic perovskite $SrRuO_3$ (SRO) epitaxially grown onto dielectric $SrTiO_3$ (STO) substrates. SRO proved to be an ideal transducer layer for large-amplitude and high-frequency coherent longitudinal acoustic phonons[29] due to its high damage threshold[30] and its fast electron phonon coupling time of ≈200 fs (Refs. 27 and 28) resulting in a quasi-instantaneous stress after photoexcitation. The lattice constants as well as the layer thickness of the two films were determined by static X-ray diffraction measurements at the ID9 beamline at the ESRF (European Synchrotron Radiation Facility, Grenoble, France) and the XPP beamline at BESSY II (Helmholtz-Zentrum Berlin, Germany) for the thin and thick film, respectively, as $c_{SRO} = 3.949$ Å and $c_{STO} = 3.905$ Å as well as $d^{(1)}_{SRO} = 15.4$ nm and $d^{(2)}_{SRO} = 94.8$ nm.

Figures 2(a) and 2(b) show a comparison of the static $\theta/2\theta$ scans around the (002) Bragg peaks of SRO and STO of the two samples (gray circles) and the simulation by dynamical X-ray diffraction theory (gray lines).[31,32] As expected, the thicker SRO film [Fig. 2(b)] exhibits a narrow and intense Bragg reflection whereas the Bragg peak of the thinner SRO film [Fig. 2(a)] is much broader and weaker. The good agreement between the experimental and theoretical diffraction curves highlights the crystalline perfection of the coherently grown SRO films on the STO substrate.[33] The acoustic impedances of SRO ($v_{SRO} = 6.312$ nm/ps,[34] $\rho_{SRO} = 6526$ kg/m^3) and STO ($v_{STO} = 7.8$ nm/ps,[35,36] $\rho_{STO} = 5117$ kg/m^3) match almost perfectly

$$\frac{Z_{SRO}}{Z_{STO}} = \frac{\rho_{SRO} v_{SRO}}{\rho_{STO} v_{STO}} = 1.03.$$

The time-resolved data in Figs. 2(c) and 2(d) were recorded at the Plasma X-ray Source (PXS) at the University of Potsdam, Germany, which provides 150 fs Cu Kα X-ray pulses with a repetition rate of 1 kHz.[37,38] For the data evaluation, a convergence correction routine was applied in order to increase the resolution in reciprocal space for the high-quality thin film samples while preserving the maximum counting statistics.[39] Compared to the high-resolution

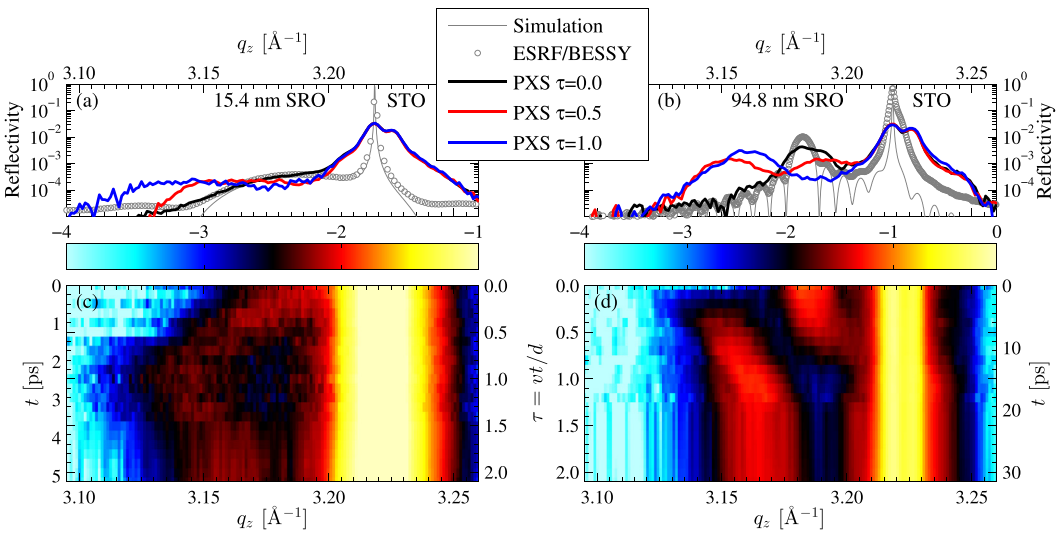


FIG. 2. Static and time-resolved $\theta/2\theta$-scans of the 15.4 nm SRO sample (left column [(a) and (c)]) and of the 94.8 nm SRO sample (right column [(b) and (d)]) around the (002) Bragg reflections of the layer at small q_z and of the substrate at larger q_z. (a) and (b) Static simulation (thin gray line) and static $\theta/2\theta$-scan (gray circles) acquired at the ESRF and BESSY II, respectively. The thick lines represent the time-resolved $\theta/2\theta$-scans measured at the PXS for different snapshots of the coherent lattice dynamics extracted from (c) and (d). [(c) and (d)] Time-resolved $\theta/2\theta$-scans measured at the PXS under incident laser fluence of $F_1 = 30$ mJ/cm^2. The color code represents the logarithmic diffracted intensity and is differently scaled, because of the much weaker reflectivity of the thin 15.4 nm SRO film. The outer y-axes represent the actual pump-probe delay t and the inner y-axes the normalized time coordinate τ.

synchrotron diffraction data, the Bragg peaks in the time-resolved measurements are significantly broadened by the resolution function of the PXS and exhibit a typical doubling due to the Cu Kα_{1+2} natural line emission.[39] The thin film samples were excited by $\lambda = 800$ nm laser pulses with a duration of 40 fs and incident laser fluence of $F_1 = 30$ mJ/cm^2 and additionally $F_2 = 20$ mJ/cm^2 only for the thicker SRO film (data not shown). In Figures 2(c) and 2(d), the inner y-axis represents the normalized time coordinate τ which is determined by the propagation time $d^1_{\mathrm{SRO}}/v_{\mathrm{SRO}} = 2.44$ ps and $d^2_{\mathrm{SRO}}/v_{\mathrm{SRO}} = 15.02$ ps of the coherent phonons across the 15.4 nm and 94.8 nm thick SRO layers, respectively.

For both samples, the transient lattice dynamics are triggered after the photoexcitation at $\tau = 0$ and reach a quasi-static state for all delays $\tau \geq 2$. In the range between $0 \leq \tau < 2$, the transient $\theta/2\theta$-scans show significantly different features for the two SRO films, namely, a continuous shift of the (002) Bragg peak towards small angles vs. a shift to larger angles combined with an intensity transfer to a peak that emerges at a smaller angle. Details about this observed splitting of the Bragg peak are discussed and related to the thermoelastic model in Sec. IV. In addition to the obvious lattice dynamics of the thin films, weak shoulders at the low- and high-q side of the (002) substrate Bragg reflection emerge at different pump-probe delays, which are best visible for the thicker SRO sample, cf. Fig. 2(d). The lattice dynamics of the substrate are beyond the scope of this work and have been discussed elsewhere in detail.[10,17,29,40]

IV. DISCUSSION

The direct correspondence between material-specific diffraction signals and the relevant transient structural parameters provides the strength of UXRD methods in following lattice dynamics on the atomic length scale in real-time. The one-dimensional Laue condition

$$q_z = n\,G = n\,\frac{2\pi}{c}, \quad n \in \mathbb{N}$$

connects the position of a specular Bragg reflection q_z to the average lattice constant c in this material along the specific crystal axis for all orders n of the Bragg peak. For small changes of the transient relative peak position $\Delta q_z/q_z(0) = [q_z(t) - q_z(0)]/q_z(0) < 1\%$ $[q_z(t) \approx q_z(0)]$, the average strain in the layer can be approximated by the relative peak shift

$$\eta_{\mathrm{lay}}(t) = \frac{c(t) - c(0)}{c(0)} \approx -\frac{q_z(t) - q_z(0)}{q_z(0)}. \tag{1}$$

For an evaluation of the experimental signal in the spirit of unitless normalized coordinates, we employ the film thickness d as obtained from the static X-ray diffraction data. In order to determine the sound velocity in the SRO film, we recall that the integrated intensity of the Bragg peaks is proportional to the thickness of the scattering layer. We know that the peak emerging at small angles corresponds to the expanding region of the thin film near the surface and plot the integrated intensity of this peak I_2 as a function of time in Fig. 3. After $t = 0$, it increases linearly until the entire layer is expanded after $t = 15.02$ ps. The two kinks in the intensity clearly mark the normalized time moments $\tau = 0$ and $\tau = 1$. The sound velocity is therefore determined as $v_{\mathrm{SRO}} = 94.8\,\mathrm{nm}/15.02\,\mathrm{ps} = 6.312$ nm/ps. As a cross check, we also plot the integrated intensity at the original Bragg peak position I_1 in Fig. 3. For both fluences, the decrease of the original Bragg peak and the increase of the emerging peak confirm this sound velocity.

The above procedure experimentally fixes the horizontal time axis in Fig. 4, where we compare the averaged normalized peak shift $\bar{\eta}_{\mathrm{lay}}(\tau) = \eta_{\mathrm{lay}}(\tau)/\eta_{\mathrm{lay}}(\tau \geq 2)$ of the experimental and theoretical results. We determine the transient positions $q_z(t)$ of the (002) SRO Bragg peaks of both thin film samples by Gaussian fits and derive the according strain in the layer using Eq. (1). For the thick SRO layer, a fit of two Gaussian functions determines the peak shift for the compressed and expanded regions of the thin film, separately. For the thinner film sample, the (002) substrate Bragg peak is subtracted from the signal in advance, because the broad thin

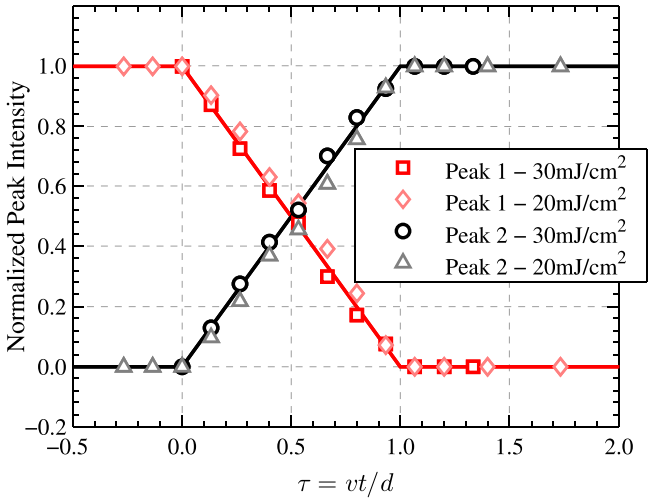


FIG. 3. Normalized integrated intensities $I_{1,2}(\tau)/(I_1(\tau)+I_2(\tau))$ of the initial (red) and emerging Bragg peak (black) of the thick SRO sample for two different excitation fluences $F_1 = 30$ mJ/cm^2, $F_2 = 20$ mJ/cm^2. Solid lines represent the normalized average strain of the compressive (red) and tensile (black) strain-regions in the layer as derived from the analytical model.

film peak merges with the substrate peak. Figure 4 shows the gradual expansion of the thinner film up to $\bar{\eta}_{\mathrm{lay}}(1) = 1.5$ (red triangles), when the tensile strain front has traveled once through this layer and gives rise to the maximum expansion. Between $1 \leq \tau < 2$ the average strain decreases to its final value $\bar{\eta}_{\mathrm{lay}}(2) = 1$. For the case of the thicker SRO layer, the experimental data for the expanded fraction of the film coincide with the thin film value $\bar{\eta}_{\mathrm{lay,exp}}(1) = 1.5$. The compressed fraction of the crystal is clearly visible in Fig. 4. It merges towards a negative average strain of $\bar{\eta}_{\mathrm{lay,comp}}(1) = -1$, however, since the corresponding intensity of the peak as a measure of the contributing thickness approaches zero, this Bragg peak vanishes just before $\tau = 1$. For a comparison to the thin film values, we calculate the center of mass (CoM) of the Bragg peak position for the thicker SRO layer (black asterisks and gray crosses). The striking agreement is an experimental verification of the the universal features of the excited lattice

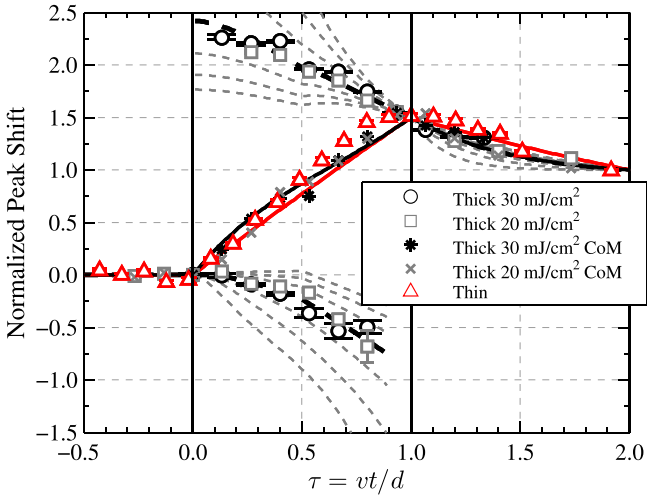


FIG. 4. The normalized peak shift $\Delta q_z(\tau)/\Delta q_z(\tau \geq 2)$ is plotted for both SRO films and fluences as open symbols (Gaussian fits) and crosses (center of mass [CoM]). The solid lines show the normalized average strain $\bar{\eta}_{\mathrm{lay}} = \eta_{\mathrm{lay}}(\tau)/\eta_{\mathrm{lay}}(\tau \geq 2)$ in the SRO layer as determined from the analytical model for the two different samples. The dashed lines represent the normalized strain of the initial and splitted Bragg peak for the thick SRO layer for different values of $\delta = d/\zeta$ ($\zeta =$ 14, 24, 34, 44, 54, 64, and 74 nm from outside to inside). The black dashed line shows the best fit for $\zeta = 44$ nm.

dynamics. It should be noted that from the data in Fig. 2 not only the normalized strain $\bar{\eta}_{\mathrm{lay}}(\tau)$ can be determined, but also the absolute value of the quasi-static average strain: $\eta_{\mathrm{lay}}(\tau \geq 2) = 0.006$ and 0.0047 for the thick layer and the two excitation fluences, respectively, as well as 0.008 for the thin layer. The normalized average strain from the thermoelastic model is plotted in Fig. 4 as black and red solid lines for the thick and thin layer, respectively.

Now we compare the experimental analysis to the analytical thermoelastic model. We can independently determine the two remaining input parameters from the experiment: The shape parameter δ is best determined from the peak shifts of the split Bragg peak of the thick layer. Figure 4 shows the results of the analytical model for different $\delta = d/\zeta$ as dashed lines. The best fit is obtained for a stress pattern decaying exponentially with $\zeta = 44$ nm. This value is therefore assumed for all simulations. The remaining parameter α can be calculated from Eqs. (A24) or (A25) in the Appendix, e.g.,

$$\eta_{\mathrm{lay}}(\tau \geq 2) = \frac{\alpha}{\delta}(1 - e^{-\delta}).$$

For the fluence range used in our experiments on the SRO thin films $\alpha \approx 0.01$.

The pronounced difference in the transient UXRD data is solely due to the different thickness of the two layers and the accordingly different shape factor δ. As discussed above, for the thicker film, $\delta > 1$, parts of the photoexcited SRO layer are transiently compressed for $0 < \tau < 1$. In principle, the Bragg peak of the thinner SRO film also exhibits a splitting due to the presence of three differently stained regions for $0 < \tau < 1$. Since all of these three regions are positively strained, the difference in the Bragg peak position is rather small and due to the small thickness of the layer and instrumental function of the PXS, the Bragg peak is initially rather broad. Thus the crystal regions with different strain only lead to a broadening of the Bragg peak. Generally, the Bragg peak width provides information about the inhomogeneous spatial strain profiles but the initial structural broadening of the film's Bragg peak and the instrumental function of the UXRD diffractometer render a quantitative analysis difficult. In a recent publication, the shape factor $\delta \sim 1$ was large enough in order to conclude on the spatial profile of the driving stresses of the lattice dynamics.[19] The experimentally derived exponential decay constant of the thicker SRO layer's stress profile $\zeta = 44$ nm (see Fig. 4) is slightly smaller than the optical absorption depth determined by optical ellipsometry as 48 nm for this sample and the accepted literature value of 52 nm.[26] This decreased value of ζ cannot be explained by transport phenomena of the photoexcited electrons in SRO which would naturally result in a broader spatial profile of the thermal stresses. For the high excitation fluences used here ($F = 20 - 30\,\mathrm{mJ/cm^2}$) non-linear absorption processes or possibly a temperature-dependent Grüneisen parameter[41] might lead to this slight steepening of the spatial stress profile in SRO.

Finally, we compare experimental $\theta/2\theta$-scans to dynamical X-ray diffraction calculation of the photoexcited crystal structure which include the instrumental resolution function of the diffractometer.[32] Figure 5 shows the excellent agreement not only of the peak positions but also of the complete Bragg peak shapes for the thicker SRO layer.

V. CONCLUSION

We introduced an analytical thermoelastic model which depends only on four parameters (the film thickness, its longitudinal sound velocity, a scaling factor, and a shape factor) for the calculation of photoexcited coherent acoustic phonon dynamics in an opaque thin film grown onto an impedance-matched transparent substrate. We presented fluence-dependent UXRD data of two SRO films of different thickness epitaxially grown on STO substrates and showed that the significantly different UXRD transients, namely, a continuous shift vs. a splitting of the (002) SRO Bragg peak, solely depend on the shape factor δ of our thermoelastic model. The variation of the shape factor δ can also be achieved by employing different excitation wavelengths instead of thin film samples of different thickness. All transient peak shifts exhibit the same universal ratio of 3/2 between the maximum shift at $\tau = 1$ and

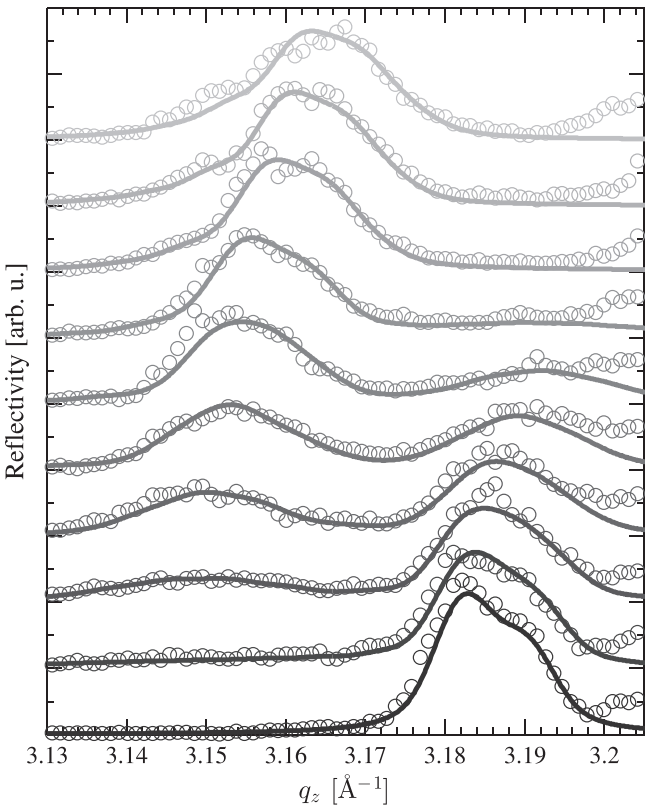


FIG. 5. The time-resolved $\theta/2\theta$-scans of the thick SRO film after $F_1 = 30$ mJ/cm^2 laser excitation are plotted as circles from 0 to 18 ps in 2 ps steps from bottom to top. The solid lines represent dynamical X-ray diffraction calculations of the strained sample as determined from the analytical solution of the thermoelastic model.

the quasi-static shift for $\tau \geq 2$. Moreover, we described a procedure to quantify all four parameters of the analytical model from the experimental data. Compared to UXRD experiments on semi-infinite crystals, the usage of thin film samples with well separated Bragg reflections of the layer and the substrate suppress complex dynamical effect and strong contributions from unexcited regions of the bulk in the UXRD experiments. Similar to the original work of Thomsen *et al.*, the assumption of negligible diffusion processes of the energy-carrying particles in the photoexcited regions is not generally valid and the thermoelastic model has to be adapted, e.g., for heat diffusion processes. Similar modifications can be applied for non-instantaneous thermal stresses after photoexcitation which requires more parameters of the model.

ACKNOWLEDGMENTS

We gratefully thank Ionela Vrejoiu for providing the samples. We thank the BMBF for funding the project via Grant No. 05K10IP1 and the DFG via Grant No. BA2281/3-1. A.B. thanks the Leibnitz graduate school "Dynamics in new Light" for financial support.

APPENDIX: THERMOELASTIC CONTINUUM MODEL FOR A THIN FILM ON A SEMI-INFINITE SUBSTRATE

We consider the 1D thermoelastic response of a thin photoexcited film of the thickness d on a semi-infinite transparent substrate which is both acoustically impedance-matched. In order to discuss the structural dynamics of the thin film, it is equivalent to consider a semi-infinite crystal

with an initial excitation profile being truncated at the depth $z = d$, e.g., the initial temperature profile. Thomsen *et al.*[8] solved this problem for a continuous initial excitation profile, i.e., for $\zeta \ll d$, where ζ represents the optical absorption depth.

First, we briefly recall the formalism introduced by Thomsen *et al.* and reformulate the according equations into the inhomogeneous wave equation by simultaneously reducing the number of parameters of the problem. We limit ourselves to a time-independent thermal excitation, i.e., we neglect diffusion of energy carriers.

The thermoelastic equations described by Thomsen *et al.*[8] have the form

$$T(z) = (1-R)\frac{Q}{A\zeta C}e^{-\frac{z}{\zeta}}\mathcal{H}(z), \tag{A1}$$

$$\sigma(z,t) = 3\frac{1-\nu}{1+\nu}B\eta(z,t) - 3B\beta T(z), \tag{A2}$$

$$\rho\frac{\partial^2}{\partial t^2}u(z,t) = \frac{\partial}{\partial z}\sigma(z,t), \tag{A3}$$

$$\eta(z,t) = \frac{\partial}{\partial z}u(z,t). \tag{A4}$$

Here, $\sigma(z,t)$, $\eta(z,t)$, and $u(z,\ t)$ are the stress tensor, strain tensor, and displacement vector, respectively, which are scalar functions for the 1D case. $T(z)$ is the time-independent temperature distribution in the sample after the initial optical excitation and $\mathcal{H}(z)$ is the Heaviside step function. All physical quantities and parameters are listed in Table I. Equations (A2)–(A4) have to be solved on a semi-infinite spatial and temporal domain ($z > 0,\ t > 0$) with the initial conditions (ICs)

$$\eta(z,0) = 0, \quad \sigma(z,0) = -3B\beta T(z), \tag{A5}$$

and the boundary condition (BC)

$$\sigma(0,t) = 0. \tag{A6}$$

In order to rewrite the above equations into an inhomogeneous wave equation, we can write the square of the sound velocity as

$$v^2 = 3\frac{1-\nu}{1+\nu}\frac{B}{\rho} \tag{A7}$$

and introduce the normalized coordinates

$$\tau = \frac{vt}{d}, \tag{A8}$$

$$x = \frac{z}{d}. \tag{A9}$$

For the case of a semi-infinite crystal without transducer layer,[8] it might be more convenient to introduce the normalized coordinates as $\tau' = vt/\zeta$ and $x' = z/\zeta$, respectively.

With the normalized coordinates x and τ Eqs. (A2)–(A4) become

$$\begin{aligned}\frac{\partial^2}{\partial\tau^2}u(x,\tau) - \frac{\partial^2}{\partial x^2}u(x,\tau) &= -\frac{3B\beta d}{\rho v^2}\frac{\partial}{\partial x}T(x),\\ \frac{\partial^2}{\partial\tau^2}u(x,\tau) - \frac{\partial^2}{\partial x^2}u(x,\tau) &= -\alpha\, d\frac{\partial}{\partial x}g(x),\end{aligned} \tag{A10}$$

where

$$\alpha = (1-R)\,\frac{3B\beta Q}{\zeta \rho v^2 AC}, \tag{A11}$$

and

$$g(x) = e^{-\delta x}\mathcal{H}(x) \tag{A12}$$

is the spatial profile of the initial temperature distribution with $\delta = d/\zeta$ as shape factor. With the introduction of the normalized dynamical displacement

$$w(x,\tau) = \frac{u(x,\tau)}{\alpha\, d} \tag{A13}$$

and the definition of the source term

$$f(x) = -\frac{\partial}{\partial x}\, g(x) \tag{A14}$$

we obtain the simplified inhomogeneous wave equation

$$\frac{\partial^2}{\partial \tau^2}\, w(x,\tau) - \frac{\partial^2}{\partial x^2}\, w(x,\tau) = f(x). \tag{A15}$$

The ICs and BC become

$$w(x,0) = 0, \quad \frac{\partial}{\partial t}\, w(x,0) = 0, \quad \frac{\partial}{\partial x}\, w(0,\tau) = 1 \tag{A16}$$

and the strain rewrites as

$$\eta(x,\tau) = \alpha \frac{\partial}{\partial x}\, w(x,\tau). \tag{A17}$$

The general solution for this problem is given by[42]

$$w(x,\tau) = \frac{1}{2}\begin{cases} p(x,\tau) + q(x,\tau) - \displaystyle\int_0^{\tau - x} \phi(s)\mathrm{d}s, & x < \tau \\ \displaystyle\int_0^{\tau}\int_{x-\tau+\vartheta}^{x+\tau-\vartheta} f(y)\,\mathrm{d}y\,\mathrm{d}\vartheta, & x > \tau, \end{cases} \tag{A18}$$

where

$$p(x,\tau) = \int_0^{\tau - x}\left(\int_0^{\tau-\vartheta-x} f(y)\,\mathrm{d}y + \int_0^{\tau-\vartheta+x} f(y)\,\mathrm{d}y\right)\mathrm{d}\vartheta, \tag{A19}$$

$$q(x,\tau) = \int_{\tau-x}^{\tau}\int_{x-\tau+\vartheta}^{x+\tau-\vartheta} f(y)\,\mathrm{d}y\,\mathrm{d}\vartheta, \tag{A20}$$

and $\phi(s) = 1$ for the BC in Eq. (A16). In general, the source term $f(x)$ may also be time dependent, e.g., if diffusion processes are not negligible, which alters the solution for $\eta(x,\tau)$ accordingly.

For the case of an abrupt end of the initial excitation profile at the depth $z = d$ or $x = 1$, we have to change the spatial profile of the initial temperature distribution $g(x)$, cf. Eq. (A12), to

$$g(x) = e^{-\delta x}(\mathcal{H}(x) - \mathcal{H}(x-1)). \tag{A21}$$

The solution is plotted in Fig. 1 for different sets of parameters. It follows from the BC in Eq. (A16) and the definition of the strain in the normalized coordinates, cf. Eq. (A17), that the amplitude of the strain at $x = 0$ is only determined by the scaling factor α

$$\eta(0,\tau) = \alpha \frac{\partial}{\partial x} w(0,\tau) = \alpha. \tag{A22}$$

Moreover, the shape of the strain pulse depends solely on the parameter δ which defines the exponential decay of the initial temperature profile $T(x)$. The temporal dimension of the phonon dynamics is scaled by the ratio v/d.

We obtain more general properties of the solution for the thin opaque layer on a semi-infinite transparent substrate by defining the integral strain in the opaque layer ($0 < x < 1$) as

$$\eta_{\text{lay}}(\tau) = \int_0^1 \eta(x,\tau)\mathrm{d}x. \tag{A23}$$

The solution at time $\tau = 1$ corresponds to the total layer strain after the coherent sound wave has traversed the layer once and it reads

$$\eta_{\text{lay}}(\tau = 1) = \frac{3}{2}\frac{\alpha}{\delta}(1 - e^{-\delta}). \tag{A24}$$

Due to the impedance matching of the layer and the substrate, for all times $\tau \geq 2$ the strain in the layer is constant since all coherent phonons have left it and the integral strains is given by

$$\eta_{\text{lay}}(\tau \geq 2) = \frac{\alpha}{\delta}(1 - e^{-\delta}) \quad . \tag{A25}$$

Thus, the ratio

$$\frac{\eta_{\text{lay}}(\tau = 1)}{\eta_{\text{lay}}(\tau \geq 2)} = \frac{3}{2} \tag{A26}$$

is independent of any physical parameter.

[1]E. Beaurepaire, J.-C. Merle, A. Daunois, and J.-Y. Bigot, Phys. Rev. Lett. **76**, 4250 (1996).
[2]B. Koopmans, G. Malinowski, F. D. Longa, D. Steiauf, M. Fähnle, T. Roth, M. Cinchetti, and M. Aeschlimann, Nature Mater. **9**, 259 (2010).
[3]U. Bovensiepen and P. Kirchmann, Laser Photonics Rev. **6**, 589 (2012).
[4]T. Huber, S. Mariager, A. Ferrer, H. Schäfer, J. Johnson, S. Grübel, A. Lübcke, L. Huber, T. Kubacka, C. Dornes, C. Laulhe, S. Ravy, G. Ingold, P. Beaud, J. Demsar, and S. Johnson, Phys. Rev. Lett. **113**, 026401 (2014).
[5]M. Först, R. Mankowsky, H. Bromberger, D. Fritz, H. Lemke, D. Zhu, M. Chollet, Y. Tomioka, Y. Tokura, R. Merlin, J. Hill, S. Johnson, and A. Cavalleri, Solid State Commun. **169**, 24 (2013).
[6]S. Wall, D. Wegkamp, L. Foglia, K. Appavoo, J. Nag, R. F. Haglund, J. Stähler, and M. Wolf, Nat. Commun. **3**, 721 (2012).
[7]C. Thomsen, J. Strait, Z. Vardeny, H. Maris, J. Tauc, and J. Hauser, Phys. Rev. Lett. **53**, 989 (1984).
[8]C. Thomsen, H. Grahn, H. Maris, and J. Tauc, Phys. Rev. B **34**, 4129 (1986).
[9]O. Wright and K. Kawashima, Phys. Rev. Lett. **69**, 1668 (1992).
[10]C. Rose-Petruck, R. Jimenez, T. Guo, A. Cavalleri, C. W. Siders, F. Rksi, J. A. Squier, B. C. Walker, K. R. Wilson, and C. P. J. Barty, Nature **398**, 310 (1999).
[11]A. Rousse, C. Rischel, and J.-C. Gauthier, Rev. Mod. Phys. **73**, 17 (2001).
[12]K. Sokolowski-Tinten, C. Blome, J. Blums, A. Cavalleri, C. Dietrich, A. Tarasevitch, I. Uschmann, E. Förster, M. Kammler, M. Horn-von Hoegen, and D. von der Linde, Nature **422**, 287 (2003).
[13]M. Bargheer, N. Zhavoronkov, Y. Gritsai, J. C. Woo, D. S. Kim, M. Woerner, and T. Elsaesser, Science **306**, 1771 (2004).

[14]H. A. Navirian, D. Schick, P. Gaal, W. Leitenberger, R. Shayduk, and M. Bargheer, Appl. Phys. Lett. **104**, 021906 (2013).
[15]R. Shayduk, M. Herzog, A. Bojahr, D. Schick, P. Gaal, W. Leitenberger, H. Navirian, M. Sander, J. Goldshteyn, I. Vrejoiu, and M. Bargheer, Phys. Rev. B **87**, 184301 (2013).
[16]A. Loether, Y. Gao, Z. Chen, M. F. DeCamp, E. M. Dufresne, D. A. Walko, and H. Wen, Struct. Dyn. **1**, 024301 (2014).
[17]Y. Gao, Z. Chen, Z. Bond, A. Loether, L. E. Howard, S. LeMar, S. White, A. Watts, B. C. Walker, and M. F. DeCamp, Phys. Rev. B **88**, 014302 (2013).
[18]D. Daranciang, M. J. Highland, H. Wen, S. M. Young, N. C. Brandt, H. Y. Hwang, M. Vattilana, M. Nicoul, F. Quirin, J. Goodfellow, T. Qi, I. Grinberg, D. M. Fritz, M. Cammarata, D. Zhu, H. T. Lemke, D. A. Walko, E. M. Dufresne, Y. Li, J. Larsson, D. A. Reis, K. Sokolowski-Tinten, K. A. Nelson, A. M. Rappe, P. H. Fuoss, G. B. Stephenson, and A. M. Lindenberg, Phys. Rev. Lett. **108**, 087601 (2012).
[19]D. Schick, M. Herzog, H. Wen, P. Chen, C. Adamo, P. Gaal, D. G. Schlom, P. G. Evans, Y. Li, and M. Bargheer, Phys. Rev. Lett. **112**, 097602 (2014).
[20]M. Nicoul, U. Shymanovich, A. Tarasevitch, D. von der Linde, and K. Sokolowski-Tinten, Appl. Phys. Lett. **98**, 191902 (2011).
[21]M. DeCamp, D. Reis, A. Cavalieri, P. Bucksbaum, R. Clarke, R. Merlin, E. Dufresne, D. Arms, A. Lindenberg, A. MacPhee, Z. Chang, B. Lings, J. Wark, and S. Fahy, Phys. Rev. Lett. **91**, 165502 (2003).
[22]D. Reis, M. DeCamp, P. Bucksbaum, R. Clarke, E. Dufresne, M. Hertlein, R. Merlin, R. Falcone, H. Kapteyn, M. Murnane, J. Larsson, T. Missalla, and J. Wark, Phys. Rev. Lett. **86**, 3072 (2001).
[23]S. Lee, A. Cavalieri, D. Fritz, M. Swan, R. Hegde, M. Reason, R. Goldman, and D. Reis, Phys. Rev. Lett. **95**, 246104 (2005).
[24]A. Cavalleri, C. Siders, F. Brown, D. Leitner, C. Tóth, J. Squier, C. Barty, K. Wilson, K. Sokolowski-Tinten, M. Horn von Hoegen, D. von der Linde, and M. Kammler, Phys. Rev. Lett. **85**, 586 (2000).
[25]A. H. Zewail, Annu. Rev. Phys. Chem. **57**, 65 (2006).
[26]P. Kostic, Y. Okada, N. Collins, Z. Schlesinger, J. Reiner, L. Klein, A. Kapitulnik, T. Geballe, and M. Beasley, Phys. Rev. Lett. **81**, 2498 (1998).
[27]C. v. Korff Schmising, A. Harpoeth, N. Zhavoronkov, Z. Ansari, C. Aku-Leh, M. Woerner, T. Elsaesser, M. Bargheer, M. Schmidbauer, I. Vrejoiu, D. Hesse, and M. Alexe, Phys. Rev. B **78**, 60404 (2008).
[28]A. Bojahr, D. Schick, L. Maerten, M. Herzog, I. Vrejoiu, C. von Korff Schmising, C. Milne, S. L. Johnson, and M. Bargheer, Phys. Rev. B **85**, 224302 (2012).
[29]M. Herzog, A. Bojahr, J. Goldshteyn, W. Leitenberger, I. Vrejoiu, D. Khakhulin, M. Wulff, R. Shayduk, P. Gaal, and M. Bargheer, Appl. Phys. Lett. **100**, 94101 (2012).
[30]M. Herzog, D. Schick, W. Leitenberger, R. Shayduk, R. M. van der Veen, C. J. Milne, S. L. Johnson, I. Vrejoiu, and M. Bargheer, New J. Phys. **14**, 13004 (2012).
[31]J. Als-Nielsen and D. McMorrow, *Elements of Modern X-ray Physics* (John Wiley & Sons, Inc., Hoboken, NJ, USA, 2011).
[32]D. Schick, A. Bojahr, M. Herzog, R. Shayduk, C. von Korff Schmising, and M. Bargheer, Comput. Phys. Commun. **185**, 651 (2014).
[33]I. Vrejoiu, G. Le Rhun, L. Pintilie, D. Hesse, M. Alexe, and U. Gösele, Adv. Mater. **18**, 1657 (2006).
[34]S. Yamanaka, T. Maekawa, H. Muta, T. Matsuda, S.-i. Kobayashi, and K. Kurosaki, J. Solid State Chem. **177**, 3484 (2004).
[35]Y. H. Ren, M. Trigo, R. Merlin, V. Adyam, and Q. Li, Appl. Phys. Lett. **90**, 251918 (2007).
[36]R. Bell and G. Rupprecht, Phys. Rev. **129**, 90 (1963).
[37]F. Zamponi, Z. Ansari, C. Korff Schmising, P. Rothhardt, N. Zhavoronkov, M. Woerner, T. Elsaesser, M. Bargheer, T. Trobitzsch-Ryll, and M. Haschke, Appl. Phys. A **96**, 51 (2009).
[38]D. Schick, A. Bojahr, M. Herzog, C. von Korff Schmising, R. Shayduk, W. Leitenberger, P. Gaal, and M. Bargheer, Rev. Sci. Instrum. **83**, 25104 (2012).
[39]D. Schick, R. Shayduk, A. Bojahr, M. Herzog, C. von Korff Schmising, P. Gaal, and M. Bargheer, J. Appl. Crystallogr. **46**, 1372 (2013).
[40]M. Herzog, D. Schick, P. Gaal, R. Shayduk, C. Korff Schmising, and M. Bargheer, Appl. Phys. A **106**, 489 (2012).
[41]C. Kittel, *Introduction to Solid State Physics*, 7th ed. (Wiley, New York, 1996).
[42]A. Bitsadzeor and D. Kalinichenko, *A Collection of Problems on the Equations of Mathematical Physics* (Mir Publishers, Moscow, 1980).